Pattern evolution of an edge-dislocation array in a lyotropic lamellar phase confined in a wedge-shaped cell: Defect formation, relaxation, and recombination

Yasutaka Iwashita* and Hajime Tanaka†
Institute of Industrial Science, University of Tokyo, Meguro-ku, Tokyo 153-8505, Japan
(Received 22 October 2007; revised manuscript received 18 February 2008; published 16 April 2008)

When a system undergoes a first-order phase transition from a disordered to an ordered state, the local energy is first minimized. This local energy minimization often prevents a system from reaching the global energy minimum state and leads to trapping in an imperfectly ordered state with many defects. In soft matter, however, a system can further relax to the global energy minimum state via slow relaxation due to its softness and fluidity. We study this relaxation process, using a lyotropic lamellar phase in a wedge-shaped cell as a model system. A lyotropic smectic liquid crystal has a large repeat unit (here, an interlayer spacing d) up to ~ 0.1 μm, and thus the motion of an individual edge dislocation in the lamellar phase can be directly observed with optical microscopy. Furthermore, a rather macroscopic spatial confinement (size h) can produce strong confinement effects, since d/h can still be large due to the largeness of d. These properties allow us to study the detailed kinetics of the relaxation process. We follow the time evolution of an edge dislocation array over 100 h from its initial stage. We reveal that the pattern evolution of an edge-dislocation array is the relaxation process of excess dislocation lines that formed initially toward the equilibrium configuration, and it is characterized by the motion of "nodes" of the topologically connected edge-dislocation network. We clarify the elementary process of this relaxation from a local to the global energy minimum state.

DOI: 10.1103/PhysRevE.77.041706 PACS number(s): 61.30.Jf, 61.30.Pq, 61.30.St, 82.70.Uv

I. INTRODUCTION

Upon a first-order disorder-order phase transition, an ordered phase is usually formed via a nucleation and growth process from a disordered phase (e.g., [1,2]). This makes it intrinsically difficult to form a perfectly ordered structure if we cannot prevent multiple nucleation [3]. Accordingly, an ordered structure initially formed via this process often has many topological defects (e.g., [2]), whose character is closely related to the type of order of the material. A mosaic polycrystalline structure is typical of such examples. Such disorder is quite harmful for various applications except for rather special cases, where defects have some useful (e.g., transport) functions. Annealing of such a structure sometimes induces relaxation toward a lower-energy structure. The formation of a more perfectly ordered structure using this annealing process is particularly important in soft matter, because its fluidity makes the strategy rather practical compared to the case of hard matter. This relaxation process can be viewed as plastic deformation of a material under internal or external mechanical stress (e.g., [4,5]). Plastic deformation of an ordered structure under stress accompanies the generation, motion, and annihilation of structural defects. Since such defects are usually localized within the length scale of the unit structure, i.e., the atomic or molecular size in solids (e.g., [6]), direct observation of their dynamics is not so easy and thus the dynamics has often been studied in terms of numerical simulations (e.g., [7]).

For studying the above problem experimentally, soft matter has a great advantage over hard matter. In ordered soft matter such as colloidal crystals [8] and lyotropic liquid crystals (LCs), we can easily observe the dynamics of an individual defect directly with optical microscopy since the system usually has a large unit structure, which also makes the dynamics very slow (e.g., [5,8]). Furthermore, a rather macroscopic spatial confinement can produce strong confinement effects. Nanoscale confinement is unnecessary for this type of soft matter, possessing large internal structures. This is because the strength of confinement is characterized by the ratio of the size of the unit structure to that of the confinement. These two factors make these systems ideal for studying the dynamics of structural defects under a geometrical confinement [5,9].

In this paper, we study the edge-dislocation array of a lyotropic lamellar phase confined in a wedge-shaped cell (Grandjean-Cano wedge) [9], focusing on the relaxation process toward its equilibrium configuration. The lamellar phase, which has a flat layered structure ("smectic" order), suffers from geometrical frustration due to the spatial gradient of the cell thickness imposed by the wedge-shaped cell. Thus, it forms an array of parallel-aligned edge dislocations, which relax the mechanical stress stemming from the nonparallel confinement. A lyotropic LC has an advantage in that even a macroscopic confinement induces strong frustration due to its large unit structure (up to ~ 0.1 μm). The equilibrium structure of an edge-dislocation array under a spatial gradient of the thickness has been studied for various LCs such as thermotropic, cholesteric, and lyotropic ones (e.g., [9–14]), and the motion of edge dislocations in an array under mechanical stress has also been studied [11,15–17]. Our main aim is to elucidate how an edge-dislocation array, which is an anisotropic network of edge dislocations, coarsens with time toward its equilibrium configuration.

The organization of this paper is as follows. In Sec. II, we review the theoretical background for an equilibrium struc-

*Present address: Max Planck Institute for Dynamics and Self-Organization, D-37073 Göttingen, Germany.
†tanaka@iis.u-tokyo.ac.jp

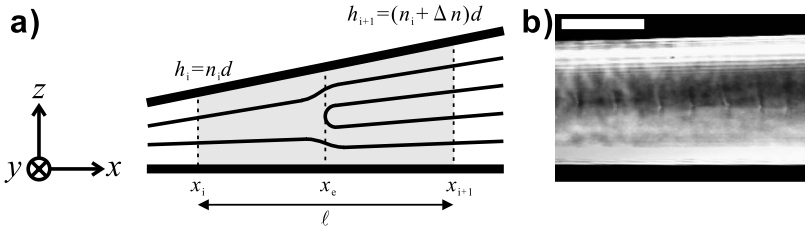

FIG. 1. (a) Schematic figure of a cross section of an edge dislocation in its array. (b) An example of the cross-sectional image of an edge dislocation array (observed with phase contrast microscopy, Olympus BH2) observed in a $C_{12}E_5$-water mixture (surfactant concentration $\phi=3.0$ wt %) at 60.0 °C. $\tan\theta=0.023$. The scale bar corresponds to 100 μm.

ture of an edge-dislocation array. In Sec. III, we describe the experimental methods, including the samples and our experimental setup and method. In Sec. IV, we describe our results on the relaxation process of an edge-dislocation array, analyze the spatial energy distribution and the characteristic elementary processes of the coarsening of an array, and discuss them. In Sec. V, we show some related interesting phenomena, such as recombination of an edge-dislocation array, an array in an isolated lamellar domain, and aggregation of onions around the boundary between a dislocation array and an onion-rich region. We summarize our study in Sec. VI.

II. EQUILIBRIUM EDGE-DISLOCATION ARRAY

Here we describe the basics of an equilibrium edge-dislocation array of a lyotropic lamellar phase (see [9] for details). A schematic figure of an edge dislocation is shown in Fig. 1(a). Here x represents the distance from the tip of a wedge-shaped cell, at which the top and bottom surface contact, and x increases toward the direction in which the cell thickness increases: in the following, x increases toward the right-hand side of the figure. We set the z axis in the direction of the cell thickness, and the y axis perpendicular to the x-z plane. Since the wedge angle between the top and the bottom surface, θ, is set to be small in our study ($\tan\theta \sim 0.02$), the thickness of the sample, h, i.e., the distance between the top and bottom surfaces, can be given as a function of x as $h \simeq x\tan\theta \simeq x\theta$.

The physical origin of an edge-dislocation array is qualitatively explained as follows. When a lamellar phase with its equilibrium periodicity d ($\simeq$layer spacing) aligns homeotropically to the two cell surfaces (i.e., layering in parallel to them), the layer compression energy increases with increase in x since the lamellar structure is stretched perpendicular to the layers with increase in the cell thickness [see the region $x_i < x < x_e$ in Fig. 1(a)]. Thus, the edge dislocation is induced to relax the layer compression energy by increasing the number of layers, at a cost of curvature elastic energy for bending the layers. The equilibrium structure minimizes the sum of these two energies.

The local minimization of the two energies determines the position of the edge dislocation, x_e. The lamellar phase is stretched in the region of $x_i < x < x_e$ and compressed in the region of $x_e < x < x_{i+1}$. The surfactant (or membrane) volume fraction $\psi \simeq \delta/d$, where δ is the thickness of the bilayer membrane. x_i and x_{i+1} are the positions at which the lamellar spacing becomes equal to the equilibrium one ($h_i=n_i d$). To be exact, the thickness $h_i=n_i d-C$, where C is almost constant with respect to i, since the layer spacing deviates from the equilibrium value near the solid surfaces (e.g., [18]). Δn is the increase in the number of layers caused by the edge dislocation, so that $|\mathbf{b}|=\Delta n d$ is the magnitude of the Burgers vector. We express the "width" of an edge dislocation by l, and then we have the relation $l=x_{i+1}-x_i=\Delta n d/\tan\theta$.

From the point view of layer compression or dilation energy, an array of elementary dislocations with $\Delta n=1$ is preferred. However, such dislocations are not observed in our system because the "edge" of the membrane costs too much energy and the confinement in our experiments is not strong enough (see Appendix A 4 and [5,19–21]). The fact that there are hardly any edges of membranes in our system implies that Δn should be an even number. Here it is worth mentioning that a similar situation is realized in other soft matter systems, such as thermotropic, cholesteric, and smectic liquid crystals: Dislocations with $\Delta n=2$ are formed except in an extremely thin part (or for a very small angle θ), due to the large core energy for $\Delta n=1$ (see Appendix A 4, and [11,13,14]).

In this work we study a thick region, i.e., $n \geq 100$. In the following, we assume $n \gg \Delta n$, since from the above relations $\Delta n/n = l/x \leq 0.01$ in our experiments (see, e.g., Fig. 4). Then, the energy of the cross section of the equilibrium structure over the length l ($=x_{i+1}-x_i$) [i.e., in the gray region in Fig. 1(a)] is composed of the energy derived from a layer spacing E_{layer} and that from the edge dislocation E_{edge} as

$$E = E_{\text{layer}} + E_{\text{edge}},$$

$$E_{\text{layer}} = \frac{B\tan\theta}{24x} l^3, \quad E_{\text{edge}} = w, \tag{1}$$

where B is the layer compression modulus and w is the energy of an edge dislocation per unit length along y. Here, $w=\frac{\kappa}{d}g$, where κ is the bending elasticity of the membrane and g is the geometric parameter of the structure of the edge dislocation (see Appendix A 1). We assume that g is constant with respect to l since g depends only weakly on Δn: The ratio of the maximum to the minimum g is estimated as $g_{\max}/g_{\min} \simeq 1.2$ for the data of all three concentrations shown in Fig. 4. Here g is numerically calculated from a simple model of edge dislocation. This allows us to assume that w is constant with respect to l (for details see Appendix A 3). Thus, the energy density per unit area in the x-y plane is obtained as

$$e(l,x) = \frac{E}{l} = \frac{B \tan\theta}{24x} l^2 + \frac{w}{l}. \quad (2)$$

Then, the equilibrium width of the edge dislocation, l^*, is determined by minimizing Eq. (2) with respect to l under the assumption of constant w, as

$$l^* = \left(\frac{12w}{B \tan\theta}\right)^{1/3} x^{1/3} = \left(\frac{12\kappa g}{Bd \tan\theta}\right)^{1/3} x^{1/3} \sim d^{2/3} x^{1/3}, \quad (3)$$

and the equilibrium number of layers, Δn^*, is related to n as

$$\Delta n^* = \left(\frac{12\kappa g \tan\theta}{Bd^3}\right)^{1/3} n^{1/3}. \quad (4)$$

We note that under the condition $n \gg \Delta n$ an edge dislocation is located almost at the middle of the width, i.e., $x_e - x_i \simeq x_{i+1} - x_e \simeq l/2$ [22].

Here we explain what we can learn from this model. From Eq. (4), Δn^* increases with an increase in $n = h/d$. In other words, Δn of an equilibrium edge dislocation is larger for weaker confinement. In principle, an edge dislocation of $2\Delta n$ has lower energy than two dislocations of Δn since the energy density around the core is dominant in w (see, e.g., [5,23]). Therefore, a small number of dislocations of large Δn are favored over many dislocations of small Δn as long as the lamellar phase is not strongly confined. This qualitatively explains the increase in Δn with increase in the total number of layers, n. We note that Δn increases from a few to tens of layers with an increase in n (see below) in our experiments, whose experimental conditions are quite different from those under which an elementary edge dislocation ($\Delta n = 1$) is observed (see Appendix A 4). Similar increases in Δn with cell thickness have been observed and discussed in various LCs (e.g., see [9,11,13,14]), but in most of those studies the change of Δn was rather small since the range of n investigated was not so large as in our experiments.

Taking thermal fluctuations of membranes into account, we use the following expressions for d, κ, and B (see, e.g., [5]):

$$d = \frac{\delta}{\psi}\left[1 + \frac{k_B T}{4\pi\kappa_0} \ln\left(\sqrt{\frac{\kappa_0}{k_B T}} \frac{1}{\psi}\right)\right], \quad (5)$$

$$\kappa = \kappa_0 - \frac{3k_B T}{4\pi} \ln\frac{d}{\delta}, \quad (6)$$

$$B = \frac{9\pi^2}{64} \frac{(k_B T)^2}{\kappa_0} \frac{d}{(d-\delta)^4}, \quad (7)$$

where $\delta = 2.76$ nm for triethyleneglycol mono-n-decyl ether ($C_{10}E_3$) and water and $k_B T = 4.14 \times 10^{-21}$ J.

As described above, the increase of the cell thickness over the distance l is given by $l \tan\theta = \Delta n d = h_{i+1} - h_i$; namely, it is equal to the magnitude of the Burgers vector $|\mathbf{b}|$. Thus, if we assume that edge dislocations are locally in equilibrium for each l, the sum of $|\mathbf{b}|$ over $0 \le x \le \Lambda$ (Λ is the total length of the sample along the x axis) should be equal to the increase in the cell thickness $\Lambda \tan\theta$ within an accuracy of one edge dislocation; namely, the sum of their magnitudes can be treated as a conserved quantity. This conservation law should hold in an actual system within the experimental error, although the existence of other kinds of small defects and impurities may lead to its weak violation.

Figure 1(b) is an example of an edge-dislocation array observed from its side. The confining surfaces are glass capillaries of diameter 1.5 mm in this case and they are parallel to the image. We can see the singular parts of the curved lamellar layers, which extend up- and downward in an arc shape from the center of each edge dislocation [5].

III. EXPERIMENT

A. Samples

The lyotropic liquid crystal we mainly used was a mixture of the surfactant molecule $C_{10}E_3$ (Nikko Chemicals Inc., BD-3SY) and water (see [24,25] for the phase diagram). We also used a mixture of $C_{12}E_5$ and water for some experiments [26,27]. These systems form various internal structures composed of surfactant bilayers [5]. In this work, two of them are important: lamellar and sponge phases. At low temperatures or high concentrations, the surfactants spontaneously form the ordered lamellar phase (L_α), which has smectic order. At high temperatures or low concentrations, on the other hand, the surfactants self-organize into the sponge structure (L_3), in which bilayer membranes separate the two bicontinuous regions of water. On length scales larger than the correlation length, the sponge phase is in the isotropic disordered state. Since the phase transition between the lamellar (ordered) and sponge (disordered) phases is weakly of first order, there exists a coexistence region between the two phases, and the lamellar phase is formed via a nucleation and growth process upon cooling.

The lamellar phase of these nonionic surfactant systems is known to be stabilized by Helfrich interactions (entropic repulsions) [28]. In the hyperswollen lamellar phase, the intermembrane spacing d is almost inversely proportional to the surfactant weight fraction ϕ: $\phi \simeq \psi = \delta/d$. Here the surfactant volume fraction $\psi = 1/[1 + \frac{\rho_s}{\rho_w}(\phi^{-1} - 1)] \simeq \phi$, where the density of water $\rho_w \simeq 0.995$ g/cm^3 and the density of $C_{10}E_3$ $\rho_s = 0.938$ g/cm^3. For example, in $C_{10}E_3$, the intermembrane spacing $d = 0.014$ μm for 20 wt % and 0.18 μm for 1.5 wt %. The characteristic length (~ 0.1 μm) is $\sim 10^3$ times larger than that of atomic systems, which means the characteristic time scale is about 10^9 times longer. This enables us to observe individual defects directly with optical microscopy [5] and to follow the kinetics in real time. In this study, we mainly used the concentration $\phi = 3$–20 wt %.

B. Wedge-shaped cells

Two types of wedge-shaped cells were prepared for horizontal and vertical (cross-sectional) observation, respectively [3]. For horizontal observation, i.e., observation through the walls which impose the spatial gradient of the cell thickness, a wedge-shaped cell was made of two flat glass plates of thickness ~ 1 mm with two spacer glass plates (the thickness of the plate was $\simeq 145$ μm) to yield a gradient of $\tan\theta \simeq 0.02$. Then, we mainly observed the region of

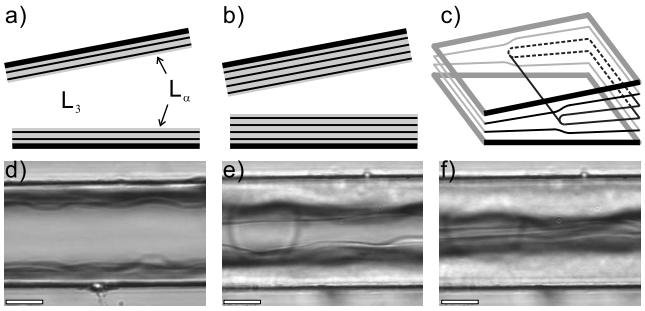

FIG. 2. Growth of the lamellar phase confined between flat glass surfaces (cross section). (a),(b) Schematic lamellar structure of growing wetting layers. (c) Schematic lamellar structure formed in a wedge-shaped cell. An edge dislocation is depicted. (d)–(f) Sequential cross-sectional images of the growing lamellar phases observed with optical microscopy (Olympus BH-2) ($C_{10}E_3$-water, ϕ =4.9 wt %, cooling rate=−0.1 K/min.). Temperatures are 34.5 °C for (d), 33.5 °C for (e), and 32.6 °C for (f). Scale bars correspond to 50 μm.

x=0–10 mm. For cross-sectional observation, we used two glass plates, whose thicknesses were about 1 mm, and made a wedge angle θ at their edge planes; they were sandwiched between two thin glass plates. We observed the inside of the cell from the side through the thin glass plates. After filling a sample, the cell was sealed with an epoxy resin (Araldite, AR-R30, Huntsman Advanced Materials). Since water evaporates very little through the sealing, we could perform experiments until ~100 h without suffering from water evaporation and the resulting concentration change.

C. Temperature control and microscopic observation

The sample temperature was controlled by a temperature-controlled stage (Linkam GS-120). We observed a sample with optical microscopy (Olympus BH-2 or BX51) and recorded images via a charge-coupled device camera (Sony, XC-EI50) to a computer. The image was digitally processed by integral average, contrast amplification, shading correction, and background subtraction with a home-made C program and commercial software (Digimo, IMAGEHYPER II). Most of the images were taken with phase contrast microscopy, and we provide information on the type of microscopy only when we use other types.

IV. FORMATION AND RELAXATION OF AN EDGE-DISLOCATION ARRAY

A. Kinetics of the sponge-to-lamellar phase transition in a wedge-shaped cell

As explained in Sec. II, an edge-dislocation array is formed as the equilibrium structure of a lamellar phase when it aligns homeotropically in a wedge-shaped cell. We formed an edge-dislocation array as follows [3]: First we heated a sample in the cell to completely transform it into the homogeneous sponge phase, which is thermodynamically stable at a high temperature. Then, we cooled it down slowly with a constant cooling rate (0.1–0.2 K/min) into the one-phase lamellar region. Upon this slow cooling, lamellar domains are formed by heterogeneous nucleation on the cell surfaces, and grow into homeotropically aligned wetting layers on the surfaces [see Figs. 2(a) and 2(b) or Figs. 2(d) and 2(e)]. Finally, further decrease of the temperature toward the one-phase lamellar region leads to direct contact of the two wetting layers around the middle of the cell, and then edge dislocations are formed in this merging process [see Fig. 2(f)]. Thus, an edge-dislocation array is formed from the thinner side of the cell and developed toward the thicker side (i.e., left to right in this paper), following the contact front of the two lamellar wetting layers (see Sec. IV for details). As can be seen in Figs. 2(e) and 2(f), the surfaces of the wetting lamellar layers are fairly smooth: the typical length scale of the undulation is ~100 μm.

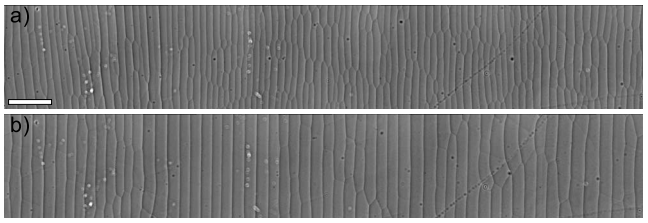

FIG. 3. An example of the relaxation process of an edge-dislocation array. (a) Part of an edge dislocation array at ≃0 h from its formation (observed with Olympus BH-2). $C_{10}E_3$ 10.0 wt %, x=1.46–2.92 mm, tan θ=0.018, 28.0 °C. (b) The array in the same region as (a) after 77 h from the formation. The scale bar corresponds to 100 μm.

B. Relaxation process of an edge-dislocation array

Figure 3(a) is an example of an edge-dislocation array formed as described above. By observing an array for a long time, we found that the initially dense array coarsens gradually toward the equilibrium one [see Fig. 3(b)].

The time development of the width distributions is shown in Figs. 4(a)–4(c). We measured the distribution along the x axis at each y at each time, and typical distributions during the coarsening process are shown in the figures. Here, since the edge width l is defined as explained in Sec. II, the "width" is estimated using the spatial modulation of the intensity amplitudes of edge dislocations in an image (see Appendix B). However, the curves in the graphs are almost identical to those of "spacings" between edge dislocations since the data are moving-averaged. In the graphs, the range of l~20–80 μm in Fig. 4(b) (3.0 wt %), 10–40 μm in Fig. 4(a) (10.0 wt %), and 10–30 μm in Fig. 4(c) (19.9 wt %). These correspond to $\Delta n = l/d \sim 4–12$, 6–24, and 12–36, respectively.

For all concentrations of 3.0, 10.0, and 19.8 wt %, the width l depends only weakly on the distance x or the thickness h (=x tan θ) just after the formation of the edge-dislocation array [see red (lowest) curves in Figs. 4(a)–4(c)]. The width increases with time, and finally the x dependence of the width starts to obey $l \propto x^{1/3}$ [see blue (uppermost) curves], which is the relation for the equilibrium width [Eq. (3)]. We believe that the initial spatial heterogeneity of the

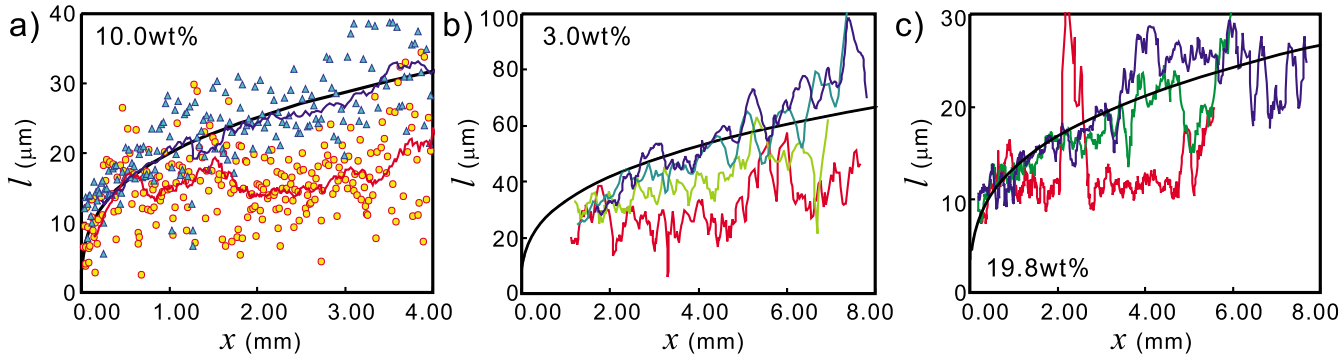

FIG. 4. (Color online) Time development of the edge width distributions in edge-dislocation arrays of $C_{10}E_3$-water. Thin curves (red, green, blue, etc.) are the moving averages of five successive widths for (b), and nine successive widths for (a) and (c). The thick smooth black curve is the theoretical curve fitted to the equilibrium widths (blue, uppermost curve). (a) $\phi=10.0$ wt %, $\tan\theta=0.018$. Circles correspond to the width of each edge dislocation at 0 h from the formation of the array and triangles correspond to that at 77 h. The theoretical curve is fitted to the widths at 77 h. (b) $\phi=3.0$ wt %, $\tan\theta=0.016$. Thin curves correspond to 1, 10, 48, and 72 h from the bottom to the top. The theoretical curve is fitted to the widths at 72 h. (c) $\phi=19.8$ wt %, $\tan\theta=0.018$. Thin curves correspond to 0, 48, and 97 h from the bottom to the top. The theoretical curve is fitted to the widths at 97 h.

width distribution, in particular, that in Fig. 4(c) at 0 h, is caused by the heterogeneous array formation process; for example, the undulation of the lamellar-sponge interface leads to the distributions of the contact time and angle between the upper and lower lamellar phases [see Figs. 2(e) and 2(f)].

This relaxation process slows down gradually, and the distribution changes only a little after ~50 h, when the array already obeys the relation of $l\propto x^{1/3}$. This suggests that the array almost reaches the equilibrium configuration. The characteristic relaxation time at which the energy of an array becomes $1/e$ is ~10 h for all three concentrations (discussed later). Since we suspect that slight evaporation of water may affect the array structure after ~100 h, we use the data only before 100 h. Possible causes of the dispersion of the measured $l(x)$ [e.g., in Fig. 4(a)] are the kinetics of coarsening (see below), the error of the intensity measurements for the estimation of l, and impurities on the cell surfaces.

It may be worth mentioning that, as can be seen in Figs. 3(a) and 3(b), an edge dislocation having a larger spacing between its neighbors generally has a larger intensity amplitude than that having a smaller spacing. This may be a consequence of the fact that the magnitude of the Burgers vector of an edge dislocation (~ its thickness) is proportional to its width (see Sec. II and Appendix B for details).

For estimating the physical properties controlling the relaxation process of an edge-dislocation array, we fitted Eq. (3) to the width distributions representing the equilibrium ones [blue (uppermost) curves in Figs. 4(a)–4(c)]. The only fitting parameter is $c=\kappa_0/k_BT$, since the layer compression modulus B can be calculated from κ. In principle, for large κ, the width of an edge dislocation l becomes large, and vice versa. This is because larger κ makes a membrane flatter, so that the energy of an edge dislocation $E_{\rm edge}$ becomes larger and the layer compression energy $E_{\rm layer}$ becomes smaller. As shown by the thick black curves in Figs. 4(a)–4(c), Eq. (3) well reproduces the data with reasonable parameter values $c=1.5-2.8$ [2.2, 1.5, and 2.8 for (a), (b), and (c), respectively], considering the scatter of the $l(x)$ data. Thus, we may say that the model in Sec. II well explains the equilibrium features of an actual edge-dislocation array, as already shown for another lyotropic lamellar phase [9].

We can explain the relaxation process as follows. At the contact of the upper and lower wetting lamellar layers, edge dislocations are formed almost instantaneously (see Sec. IV D). Thus, the elastic relaxation of the deformation of lamellar spacing (corresponding to $E_{\rm layer}$), which is caused by the small angle between the wetting layers, can proceed only locally around the contact interface. Thus, the balance between the elastic deformation energy $E_{\rm layer}$ and the energy of edge dislocation $E_{\rm edge}$ depends solely on the local contact angle between the two lamellar surfaces, so that the width (or spacing) of edge dislocations is rather independent of the cell thickness h (or the position x). However, this also means that too many edge dislocations are formed compared to the equilibrium edge-dislocation array, in which the elastic deformations of lamellar spacings are relaxed over the whole system. As a result, the initial array gradually relaxes toward the equilibrium one via its coarsening.

C. Coarsening kinetics

1. General features of kinetics and layer configurations

In the above, we described the relaxation process of the whole edge-dislocation array. Here we describe the kinetics of the relaxation, or the coarsening of the network of edge dislocations, focusing on the elementary process. In addition to direct observation of the coarsening process, we also estimate the two-dimensional spatial distribution of energy using Eq. (2), and discuss its temporal change. Figure 5 is such an example: Figs. 5(a)–5(f) show the optical microscopy images, whereas Figs. 5(a)–5(f) show the calculated energy distributions. For calculating the energy density in two dimensions, we estimate the edge width l of an edge dislocation just by averaging the two spacings between it and its neighbors for simplicity (see Appendix B). Here we also ignore the difference between the lamellar structures around the

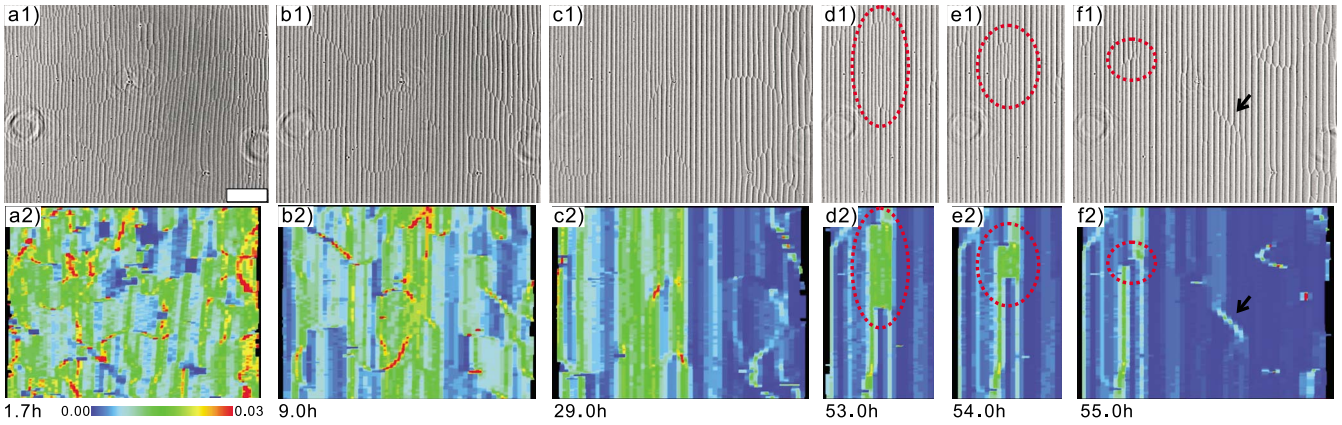

FIG. 5. (Color online) Time development of an edge-dislocation array [(a1)–(f1)] and its energy distribution [(a2)–(f2)]. $C_{10}E_3$-water, $\phi=10.0$ wt %, 31.0 °C, tan $\theta=0.017$, and $h=52$ μm ($x=3.05$ mm) at the center of the images except for (d) and (e). The elapsed times after the sample temperature reaches the one-phase lamellar region (28.0 °C) are 1.7, 9.0, 29.0, 53.0, 54.0, and 55.0 h, respectively, from (a) to (f). The dotted red circles indicate the shrinking region of higher energy. The color bar represents the energy density (the unit is 10^{-6} J/m^2. The scale bar in (a1) corresponds to 200 μm.

"node" of the network of edge dislocations and the structures of parallel-aligned edge dislocations, and simply apply the analysis in Sec. II to the calculation. In Fig. 5, we can clearly see that the edge width of the edge-dislocation array increases with time and the energy decreases while approaching the equilibrium state.

First we describe the basic characteristics of the kinetics elucidated from our observations and analyses.

(1) There is neither breaking of the network of edge dislocations nor creation of a new node. We never observed the following processes: (a) Two separate edge dislocations come closer and coalesce (and make two new nodes); (b) an edge dislocation splits into two parallel ones (and also makes two new nodes); (c) an edge dislocation breaks up and shrinks in length.

(2) Thus, the coarsening takes place only when nodes, which are created upon the initial formation of an array, move in the direction parallel to the edge dislocations (y direction) to reduce the number of dislocation lines. Thus, a domain in which edge dislocations align parallel without nodes grows in the y direction.

Points 1a and 1b are rather evident from the structure of an edge dislocation in the array described in Sec. II. As can be seen from Fig. 1(a), the position of an edge dislocation x_e is fixed to minimize the deformation energy of interlamellar spacings exerted by the angled cell walls. Thus, the position x_e is not affected by the structures of neighboring edge dislocations (e.g., the widths l). In other words, each edge dislocation is almost fixed to the local equilibrium position under the existence of the cell walls, and it does not interact with neighboring dislocations in a direct manner. Point 1c indicates that an edge dislocation in the lamellar phase is stable. For point 2, we can confirm, e.g., in the energy distribution shown in Fig. 5(c), that a parallel-aligned array domain, in which the width (or energy) is almost constant, grows only in the y direction.

Next we discuss the structure of lamellar layers around a node, on the basis of the model structure of Fig. 1(a) [or Fig. 2(c)]. First we consider the motion of a node, i.e., a zipperinglike mode, by which two edge dislocations coalesce into one [see Fig. 6(a)]. Upon this coalescence, the sum of the magnitudes of the Burgers vectors $|\mathbf{b}|$ must be conserved [see the layer structure in Fig. 1(a) or Fig. 2(c)]. As shown in Fig. 6(a), thus, when two dislocations of $|\mathbf{b}|=\Delta n_1 d$ and $|\mathbf{b}|=\Delta n_2 d$ coalesce into a dislocation, we should have the relation $|\mathbf{b}|=\Delta nd=(\Delta n_1+\Delta n_2)d$. In the figure, h_i is the thickness at which the equilibrium lamellar spacing is commensurate with the thickness ($h_i=n_i d$, $i=1-3$). Thus, $h_2=h_1+\Delta n_1 d$ and $h_3=h_2+\Delta n_2 d=h_1+(\Delta n_1+\Delta n_2)d$. Figure 6(b) is a schematic figure of layer structures before and after the node, in which $\Delta n=6$, $\Delta n_1=2$, and $\Delta n_2=4$. Figure 6(a) also explains the above statement that the motion of the node does not affect the positions of neighboring independent edge dislocations (e.g., the two neighboring edge dislocations at the left of h_1 and at the right of h_3), since h_1 and h_3 are not affected by the coalescence. This conservation of the total Burgers vector is also supported by the monotonic relation between the width of an edge dislocation and its intensity amplitude (see Appendix B). We believe that this picture of layer structures around a node should be basically correct, since actual patterns around nodes are quite consistent with this picture [see, e.g., Fig. 6(h)].

2. Elementary process of the coarsening

An edge-dislocation array evolves with time, reflecting the topology of the network of edge dislocations and anisotropy imposed by the spatial gradient of the thickness of the wedge-shaped cell. Here we explain the characteristic kinetics in each stage of the relaxation process in more detail. As already mentioned, the motion of nodes toward the region of denser edge dislocations is a fundamental process of the array relaxation (coarsening), i.e., the motion always decreases the total length (or local number) of dislocations. Neither breaking of an edge dislocation nor creation of new nodes are observed. The simplest process is the "2 vs 1 node" mode toward the two edge dislocations [Fig. 6(a)].

Figures 6(c) and 6(d) demonstrate the topological change of the network of edge dislocations by the 2 vs 1 node mode.

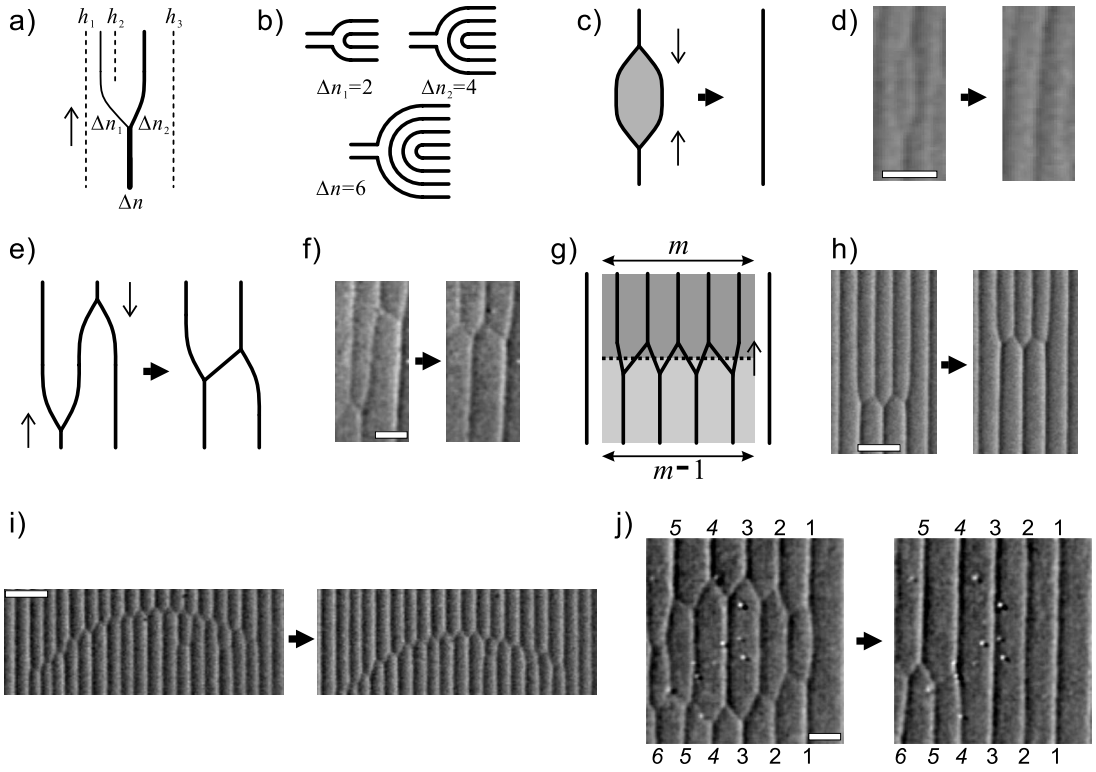

FIG. 6. Elementary processes of the coarsening of an edge-dislocation array. Thick arrow indicates the temporal change of a pattern. Thin arrow indicates the direction of the motion of a node (nodes) of edge dislocations. All optical microscopy images are for $C_{10}E_3$-water. (a) A node of edge dislocations. The magnitude of the Burgers vector $|\mathbf{b}|=\Delta nd$, $\Delta n_1 d$, and $\Delta n_2 d$. Note that $\Delta n_1 < \Delta n_2$. The dashed lines indicate the positions where the sample thicknesses are commensurate with the equilibrium lamellar structure [see Fig. 1(a)]. (b) Schematic figure of the cross-sectional view of edge dislocations in (a). (c) An elementary process of topological relaxation of an edge-dislocation network. Two nodes of opposite orientations collide and the network relaxes into a single edge dislocation. (d) Example of the process (c). The closed region in the left image disappeared in ~3.5 min. ϕ=3.0 wt %, 28.0 °C, tan θ=0.018, and h=10 μm (x=0.55 mm). (e) Pairing of two nodes of opposite orientations. (f) Example of the process (e). The right figure is at 60 min later than the left one. The sample is the same as (d). (g) Aligned nodes between domains of edge dislocations with different numbers of dislocations (m and $m-1$) or different widths. Here, 5 vs 4 aligned nodes are depicted. (h) Example of the motion of aligned nodes. The 4 vs 3 nodes moved by 70 μm from the left to right in 30 min (velocity=2.3 μm/min). ϕ=10.0 wt %, 31.0 °C, tan θ=0.017, and h=54 μm (x=3.16 mm). (i) Another example of moving aligned nodes. Here the 18 vs 17 aligned nodes moved by 29 μm in 100 min (velocity=0.29 μm/min). ϕ=10.0 wt %, 31.0 °C, tan θ=0.017, and h=18 μm (x=1.05 mm). (j) Example of the collision of two aligned nodes. Three edge dislocations from the right (indicated by the numbers 1, 2, and 3) relax into straight ones (without nodes), whereas the others relax into aligned nodes. The sample is the same as (d). All scale bars correspond to 50 μm.

In this process, two nodes of opposite orientations move to the directions that reduce the number of dislocations, i.e., approach each other, and finally the structure relaxes into a single straight edge dislocation. Note that no topological change of lamellar layers takes place in this process. Molecules in the gray region in Fig. 6(c) are not confined there since layers are continuous between the inside and outside. This type of coarsening process, i.e., the disappearance of an independent closed pattern of edge dislocation, is fairly rare and observed only in the early stage of the relaxation process. This process is also less frequent for higher ϕ; for example, it was never observed for ϕ=19.9 wt %.

On the other hand, if two 2 vs 1 nodes of opposite orientations are connected with only one of the two dislocations, a topological change of the network does not occur; they simply form a pair of nodes [see Figs. 6(e) and 6(f)]. This pairing, however, leads to a decrease in the number of dislocations in the array. For example, in Fig. 6(e), the edge dislocation shrinks to form the 2 vs 2 nodes structure. As can be seen in the figure, the "pair" structure is energetically more stable than that before pairing, since the widths (or spacings) of the edge dislocations are increased by pairing. Thus, the number of nodes in the state of "aligned nodes" increases as the coarsening proceeds. Figure 6(g) is an example of 5 vs 4 aligned nodes, in which seven 2 vs 1 nodes are aligned. On the other hand, if we focus on the domain of parallel-aligned edge dislocations, a state of aligned nodes can be regarded as a mismatched boundary between the two array domains, both of which are parallel-aligned edge dislocations but whose positions and widths are different. For example, in Fig. 6(g), the state of the aligned nodes is a kind of a boundary structure between the upper domain of the width $l=L/m$ and the lower one of $l=L/(m-1)$ (here L is the length of the aligned nodes).

The orientation of the aligned nodes depends on the relative positions of the edge dislocations between both sides: If

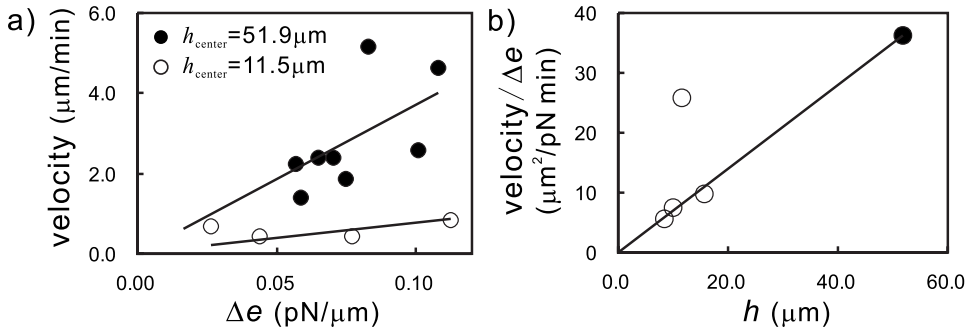

FIG. 7. Velocities of aligned nodes ($C_{10}E_3$-water, ϕ=10.0 wt %, tan θ=0.017). (a) Velocities of aligned nodes plotted against the energy density differences across them (Δe). Filled and open circles correspond to the velocity at thickness $h \simeq 51.9$ and at $\simeq 11.5$ μm, respectively. Strictly speaking, the thickness h at each dislocation depends on its horizontal position x. The lines are fitted to the data. (b) Velocity/Δe ("mobility") plotted against h. The open circles are the same data in (a), plotted against their thicknesses at the positions x, whereas the filled circles represent the average of the data of the filled circles in (a). The line is to guide the eye.

the edge dislocations at one side are not in the middle of those at the other side, the aligned nodes (the boundary) incline from the x direction [see, e.g., the arrowed boundary in Fig. 5(f)]. Thus, long aligned nodes become arc shaped when the two sides have different l [see, e.g., Fig. 6(i)].

According to our observation of the coarsening process, these m vs $m-1$ aligned nodes (mismatched boundary) move toward the region of m dislocations to decrease the total length (or local number from m to $m-1$) of dislocations as in the case of 2 vs 1 node. This increases the widths of edge dislocations and decreases the elastic energy toward the equilibrium structure of the array. Here, as mentioned above, the average of the number m of m vs $m-1$ nodes increases with time by pairing of nodes [see, e.g., Figs. 6(h) and 6(i)], although all nodes are 2 vs 1 nodes just after the edge-dislocation array is formed.

In this paper, we do not take m to m nodes into account since (i) they play little role in the coarsening and (ii) their population is much less than that of the m vs $m-1$ nodes according to our observation. Points (i) and (ii) may be explained as follows. (i) The motion of m to m nodes does not change the total length (and local number) of the dislocations. The small difference in the energy between the two sides means the motion should be very slow. (ii) The m to m nodes require similar and almost constant l for both sides, especially for large m. However, such conditions are scarcely satisfied due to the spatial heterogeneity of l [see Figs. 4(a)].

Here we stress that the topology of the network is not changed by the motion of a node or aligned nodes alone. It changes because of collision of two aligned nodes, as described for two 2 vs 1 nodes in Fig. 6(c). Figure 6(j) is such an example observed. When the two aligned nodes approach and collide, the nodes relax to the straight dislocation lines as in Fig. 6(c), if the upper and lower domains of the two aligned nodes are commensurate, i.e., the positions and widths of edge dislocations are the same (see the numbered dislocations 1, 2, and 3 in the figure). However, aligned nodes remain if they are not commensurate (see 4, 5, and 6).

Here we have shown that the relaxation (coarsening) process of an edge-dislocation array occurs via the motion of m vs $m-1$ aligned nodes, the increase of m by pairing, and the disappearance of nodes by their collision (topological relaxation).

3. Dynamics of aligned nodes

Next we focus on the dynamics of aligned nodes. From our observation, it turns out that the motion of m vs $m-1$ nodes becomes slower for larger m. This can be explained by the decrease of the driving force of the motion with an increase in m: For simplicity, we consider the m vs $m-1$ nodes between the array domains of constant widths (or spacings) as in Fig. 6(g). Here the width l increases from $l_m=L/m$ to $l_{m-1}=L/(m-1)$ by the motion of m vs $m-1$ nodes. Thus, the energy density per area decreases from $e(l_m)$ to $e(l_{m-1})$. This energy density difference $\Delta e=e(l_m)-e(l_{m-1})$ should drive the motion. The difference in l for the same width, i.e., $\Delta l=l_m-l_{m-1}=L/m(m-1)$, decreases with an increase in m. Thus, Δe also decreases with increasing m, which leads to a decrease of the velocity of the motion. In our experiments, however, the width l also depends on array domains, and thus the velocity must be determined by the balance between the energy density difference (not solely by m) and the mobility of m vs $m-1$ nodes.

Upon the motion of edge dislocations, the medium behaves as a fluid made of membranes and intermembrane liquid, and thus the flow in a lamellar phase has a two-dimensional nature [29]. If we assume that the mobility of the unit length of aligned nodes is the same for any aligned nodes, then the velocity of aligned nodes at a certain thickness should be proportional to its energy density difference. Based on this simple argument, we plot the velocities of aligned nodes at a certain thickness range against their energy density differences Δe in Fig. 7(a). To estimate Δe, we average each energy density of both sides of an aligned node, for which the energy density is calculated from the spacings between the edge dislocations, and then calculate Δe. Here we made these analyses for two different thicknesses of the cell. The velocity increases with an increase in Δe. We speculate that the slower motion in a thinner region is due to the larger effective viscosity because of the stronger confinement. Note that both membranes and the intermembrane liquid flow along the membrane. Thus, the effective viscosity of the mixture increases with a decrease in the gap between the solid walls, which impose a nonslip boundary condition on the flow.

An interesting example of this type of motion is shown in Fig. 5. In the area circled with the red dotted line, the two

aligned nodes approach each other to make the high-energy area smaller [see the bright (green) area in the lower figures]. However, since the energy difference between the two sides of the aligned nodes finally becomes small, it moves little after Fig. 5(f). Since the number of edge dislocations is locally doubled around the aligned nodes, the aligned nodes have a higher energy than the parallel edge dislocations, and the higher energy works as line tension in the two-dimensional array structure. However, the aligned nodes cannot relax spontaneously since the topological change (i.e., recombination of the lamellar layers) required for the relaxation is not allowed. Actually, we have never observed such a spontaneous relaxation process. In the later stage of the relaxation process of the edge-dislocation array, the elastic energy almost relaxes to the equilibrium one. Thus, the motion of the aligned nodes is almost "frozen." Accordingly, long aligned nodes often exist near the equilibrium state despite its high energy cost, because collision between aligned nodes, which is the only way for the edge-dislocation network to further relax energetically, rarely occurs. The arrowed aligned nodes in Fig. 5(f) are such an example.

Figure 7(a) shows the relation between the velocity of aligned nodes and the energy difference across them, Δe. There is a positive correlation, but with a large scatter of data points. Here we discuss a possible origin of the scatter of data in Fig. 7(a). The actual velocity of the aligned node is determined by the balance between its mobility and the energy difference across the aligned node, as described above. The dissipation associated with the motion originates from the change of layer structures accompanied by the motion of a node or nodes ["zippering" of edge dislocations; see Figs. 6(a) and 6(b)]. Thus, the dissipation should depend on the structural features around a node or nodes such as the length of aligned nodes L and Burgers vectors $|\mathbf{b}|$ of the edge dislocations. Although the kinetic effects of these factors are interesting, it is difficult to extract their effects from our experiments because they are overwhelmed by the scatter of the data in Fig. 7. We confirmed that the motion sometimes slows down or is even pinned by impurities sticking on the cell surfaces, which may be the main cause of the large scatter of the data. On the other hand, the effects of $|\mathbf{b}|$ may be rather weak, since the motion of aligned nodes is controlled by a sort of "averaged" $|\mathbf{b}|$ of the many edge dislocations in it. Furthermore, the thickness dependence of the averaged $|\mathbf{b}|$ of an array is also not very large; see, e.g., the change in l in Fig. 4(a) from $h \simeq 11.5$ to 51.9 μm (note that $|\mathbf{b}| \propto l$ and $h \simeq x \tan\theta$).

In Fig. 7(b), we plot the ratio of the velocity to Δe, which corresponds to the mobility, against the thickness h to show the thickness dependence of the motion. Although the data are scattered, the basic tendency that the motion is more damped in a thinner region is evident.

We have shown that the elementary process of the coarsening of an edge-dislocation array is the motion of aligned nodes driven by the energy difference across them. Here we estimate how the total energy of an edge-dislocation array (per unit length along the y axis) relaxes with time as the coarsening proceeds. Figure 8 summarizes the results obtained from the same experiments shown in Fig. 4 (note that curves at all times are not shown in Fig. 4 to avoid overlapping). The total energy is estimated again on the basis of the model in Sec. II, for the width distribution of an edge-dislocation array (not for the spacing distribution). Here it is worth noting that the density (or number) of nodes is not directly related to the energy of an edge-dislocation array; see, e.g., Fig. 6(e), where the energy relaxes while keeping the topology of the network. Since the estimated width data scatter, e.g., due to the scatter of the intensity amplitude (see Sec. IV B), we use the moving average of the width for the calculation of the energy. It is a subtle issue how many data points should be averaged to estimate the energy properly. Since this affects the absolute value, we do not discuss it, but instead we consider how the energy changes relatively with time. In Fig. 8, we normalize the excess energy density per unit length along the y axis, $\Delta E_{mv} = E_{mv} - E^*$, by the equilibrium one E^*, which is calculated using Eqs. (2) and (3) from the fitted theoretical curves in Fig. 4.

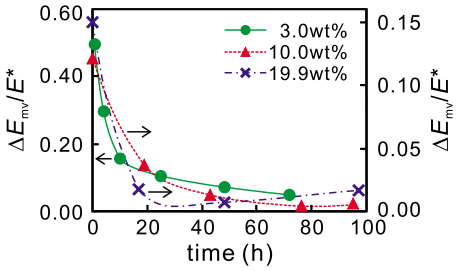

FIG. 8. (Color online) Time dependences of the estimated energies of edge dislocation arrays in $C_{10}E_3$-water. Filled circles are for $\phi = 3.0$ wt % and $\tan\theta = 0.016$, filled triangles are for $\phi = 10.0$ wt % and $\tan\theta = 0.018$, and crosses are for $\phi = 19.9$ wt % and $\tan\theta = 0.018$. The curves are to guide the eye (smooth connections of the data points). The excess energy density per length is normalized by the equilibrium energy density E^* ($E^* \simeq 26$ pN for 3.0 wt % in $x \simeq 1.3-6.0$ mm, 350 pN for 10.0 wt % in $x \simeq 0.05-3.00$ mm, and 2000 pN for 19.9 wt % in $x \simeq 0.19-5.00$ mm).

An interesting point is that the energy relaxation process does not depend on the concentration, i.e., the characteristic relaxation time scale is ~ 10 h for all the concentrations studied. Here we note that the behavior for $\Delta E_{mv}/E^* < 0.1$ suffers from estimation errors due to the large scatter of the width estimation (cf. Fig. 4) and should not be taken seriously.

D. Formation kinetics of an edge-dislocation array

Next, we describe how edge dislocations are formed in the beginning. As already shown in Fig. 2, the lamellar-

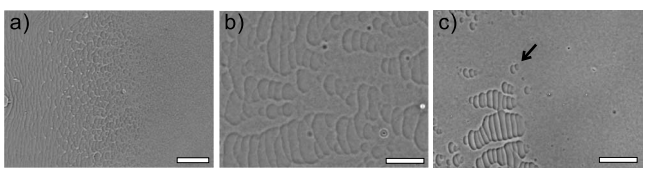

FIG. 9. Images upon the formation of edge-dislocation arrays in $C_{10}E_3$-water (observed with Olympus BH-2). (a: $\phi = 3.0$ wt %, 29.0 °C (−0.1 K/min), $h \simeq 45$ μm, and $\tan\theta = 0.018$. (b) $\phi = 10.0$ wt %, 30.8 °C (−0.2 K/min), $h \simeq 54$ μm, and $\tan\theta = 0.018$. (c) $\phi = 19.8$ wt %, 33.1 °C (−0.1 K/min), $h \simeq 69$ μm, and $\tan\theta = 0.017$. The scale bars correspond to 200 μm for (a) and 100 μm for (b) and (c).

sponge interfaces of the lamellar wetting layers, which are homeotropically aligned on the upper and lower inner surfaces of the wedge cell, start to contact from the edge of the wedge-shaped cell ($x \sim 0$) toward larger x while forming edge dislocations. In Fig. 9, we show how edge dislocations are formed upon the contact of the two interfaces. The samples are in the process of slow cooling toward a temperature that is several kelvins into the lamellar one-phase region from the phase boundary. The widths of the initially formed edge dislocations are smaller for a higher concentration, as can also be seen in Fig. 4. We also confirmed that the formation of edge dislocations proceeds from a thinner part (left) to a thicker part (right) for all the concentrations. This formation kinetics obviously depends on the concentration: At a high concentration [see Fig. 9(c), 19.8 wt %], the formation of an edge-dislocation array is clearly nucleation-and-growth-like, i.e., a domain of the array is formed and then grows. Thus, the formation process of the array is spatially inhomogeneous. Furthermore, the domain shape is anisotropic, longer in the x direction. At a low concentration, on the other hand, the array is formed rather homogeneously from left to right at a similar thickness [see Fig. 9(a), 3.0 wt %]. The formation kinetics also depends on the thickness of the sample, i.e., the array is formed more homogeneously at a thinner part for the same concentration. Here the gradual undulations of the wetting layers (see, e.g., Fig. 2) should also affect the heterogeneity of the formation kinetics. We note that the elementary process is the topological transformation of the sponge membranes confined in the narrow space between the wetting lamellar layers to the lamellar structure. Although the origin of the anisotropy of the array domains in Figs. 9(b) and 9(c) is not so clear, it might reflect the anisotropic undulation of the lamellar-sponge interface, reflecting the thickness gradient direction of the cell.

After the wetting lamellar layers are in contact (or are bridged), an edge-dislocation array is formed almost instantaneously, when the domain size exceeds the initial width of an edge dislocation [see the arrowed domain in Fig. 9(c)]. This suggests that edge dislocations are formed by the local angle between the interfaces of wetting layers at the contact, not by the angle of the wedge cell itself. The deformation of the lamellar spacing is local at the contact, i.e., the deformation does not reach the whole thickness of the cell. This local deformation is effectively the same as the edge-dislocation array in a thin region, at which the deformation is limited by the small thickness. We believe that this is the reason why the width of an initial edge-dislocation array is almost independent of the cell thickness and is smaller than the equilibrium width.

In addition, from the observations, the dislocations formed first have minimum widths in the coarsening process. Strictly speaking, they should be narrower than those at 0 h in Fig. 4 since the data are taken after some minutes from their formation. The analyses in Sec. II tell us that the first dislocations are not necessarily the smallest ("elementary") dislocations of $\Delta n=2$. The dislocations formed first should depend on the local contact angle between the two lamellar wetting layers. Actually, in Fig. 9(c) the spacings of the first dislocations are larger than that of the elementary dislocation $l(\Delta n=2)=1.6$ μm. Here it should be noted that the spacings in Fig. 9 do not necessarily reflect the Burgers vectors directly, since the system is out of equilibrium even locally.

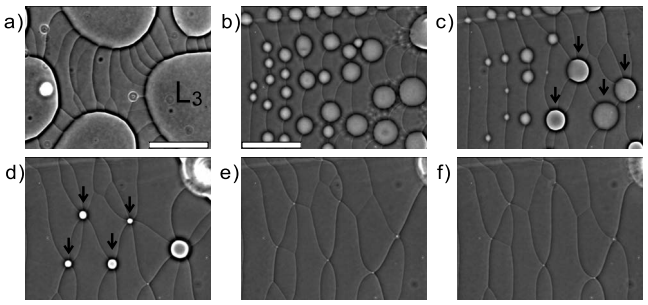

FIG. 10. Recombination of edge dislocations by nucleation of the sponge phase (L_3) ($C_{10}E_3$-water, $\phi=10.0$ wt %, Olympus BX51). (a) Lamellar phase with an edge-dislocation array coexists with large sponge droplets. $\tan\theta=0.016$. (b)–(f): Sequential images of the recombination process. Initially, nucleation of the sponge phase is induced by heating and then the sample is gradually cooled down to the one-phase lamellar region (-0.1 K/min). $\tan\theta=0.018$. (b): 35.9, (c) 35.5, (d) 35.0, (e) 35.0 °C, 7 min from (d), and (f) 35.0 °C, 15 min from (d). x position of the images was slightly shifted between (c) and (d) (the corresponding sponge droplets are indicated by arrows). The scale bars correspond to 100 μm.

E. Summary of the relaxation of an edge-dislocation array

In this section, we have shown that the coarsening of an edge-dislocation array is the relaxation process toward its equilibrium structure, which is described by the model in Sec. II. From direct observation over a long period of time, we successfully relate the kinetics of the coarsening to the time development of the two-dimensional energy distribution based on the model of the equilibrium structure. In particular, we reveal that the elementary process of the coarsening is the motion of m vs $m-1$ aligned nodes, and that the motion is driven by the energy difference across aligned nodes to decrease the length (and number from m to $m-1$) of edge dislocations. Topological relaxation of an array, which is a network of edge dislocations, is induced by the collision of two aligned nodes. Finally, the characteristic relaxation time of the total energy is ~ 10 h, which is independent of the concentration.

V. OTHER RELATED PHENOMENA

In the following, we describe some other interesting phenomena observed in our experiments.

A. Recombination of edge dislocations by nucleation of sponge droplets

When a lamellar phase with an edge-dislocation array is heated up into the lamellar-sponge coexistence region, the sponge phase selectively nucleates on edge dislocations [Fig. 10(b)]. This is because structural defects are in a high-energy state and thus act as nucleation agents to induce heterogeneous nucleation. Such selective nucleation of the isotropic phase on defects is generally observed in melting of an or-

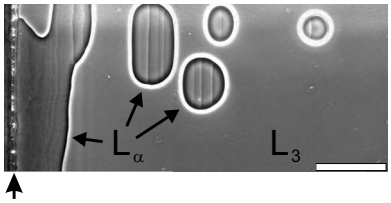

FIG. 11. Edge-dislocation arrays formed in isolated lamellar domains coexisting with the sponge phase ($C_{10}E_3$-water). The image was taken at 40.9 °C with Olympus BX51. The sample of $\phi=10.0$ wt % and tan $\theta=0.018$ was heated from 34.0 to 40.6 °C with a rate of 20.0 K/min, and then it was slowly heated to 40.9 °C. The contact line of the two glass plates, i.e., where $x=0$, is indicated by the leftmost arrow below the image. The scale bar corresponds to 100 μm.

dered phase (e.g., [25,30]). We found that edge dislocations tend to align perpendicular to the lamellar-sponge interface [Fig. 10(a)]. This may reflect the membrane organization at the lamellar-sponge interface, although the details should be clarified in the future.

Using this characteristic, we can transform parallel-aligned edge dislocations back into the network: First, we form sponge nuclei by heating and make them grow so that several edge dislocations are connected to a sponge nucleus [Fig. 10(b)]. Next, when the temperature is lowered back into the lamellar one-phase region, the edge dislocations are connected at a node, following the shrinking sponge nucleus [Figs. 10(c)–10(e)]. Finally, the topology of an edge-dislocation array is changed to a network where edge dislocations are connected [Fig. 10(f)].

B. An edge-dislocation array in an isolated lamellar domain

In the above, we show that isolated sponge droplets are formed at a temperature where the sponge phase is the minority phase. On the other hand, when a sample is heated rapidly to the temperature at which the lamellar phase is the minority phase, an isolated lamellar droplet with an edge-dislocation array is formed (Fig. 11). In this case, isolated lamellar domains with the arrays are surrounded by the sponge phase. Note that there are no macroscopic wetting layers of the lamellar phase on the cell surfaces, although a few prewetting lamellar layers should exist on the cell surfaces (e.g., [19]). This situation is essentially different from the array domains shown in Sec. IV D [cf. Fig. 9(c)]. Furthermore, the shape of the lamellar domain is anisotropic, longer in the direction parallel to edge dislocations (y direction), in particular, in a thin region. This is also different from the array domains in Fig. 9(c), which are longer in the x direction. We speculate that this anisotropic shape (shorter in the gradient direction) is preferred to lower the elastic deformation energy, although further detailed analysis is desirable.

C. Aggregation of onions around a boundary between an edge-dislocation-array region and an onion-rich region

As shown in our previous papers [3,31], the "onion" phase, which is the lamellar phase composed of multilamellar vesicle structures, is formed in the region where the cell thickness is thicker than the characteristic thickness. This characteristic thickness is determined by the competition between the rate of the temperature cooling and the homogenization of the depletion zone created by the nucleation and growth process via diffusion [3]. When we observed the boundary between the homeotropically aligned lamellar region (i.e., the region of an edge-dislocation array) and the onion-rich region, we found that the onion structures migrate toward a thicker region (toward the right) and thus aggregate (Fig. 12). We speculate that onion structures effectively attract with each other in the flat lamellar structure, since the spherical structure of onion is incommensurate with the lamellar structure and accompany the deformation of the smectic order, which results in an elastic energy cost. This elastic energy cost can be reduced by aggregation of onions. The smaller elastic distortion in a thicker part may select the direction of motion of onions toward the thicker region.

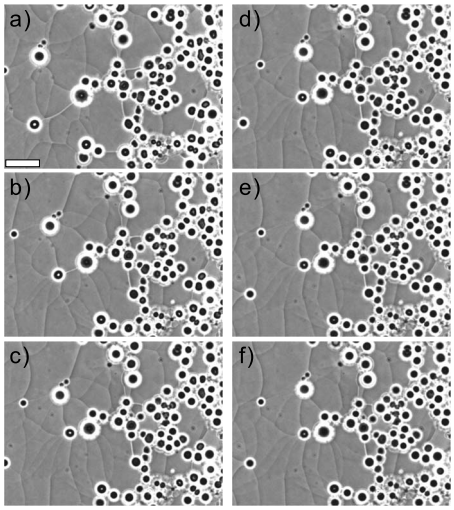

FIG. 12. Sequential images of onion aggregation around the boundary between the homeotropic lamellar region and the onion-rich region ($C_{10}E_3$-water, $\phi=10.0$ wt %, tan $\theta=0.010$). The sample was quenched from the one-phase sponge region to 28.0 °C with a rate of −20.0 K/min. (a) is about 10 min after the temperature reached 28.0 °C, and the interval between the images is 30 min. The scale bar corresponds to 100 μm.

VI. SUMMARY

We directly observed the formation of an edge-dislocation array and its coarsening (relaxation) in a wedge-shaped cell. By measuring the edge width distribution of the array, we confirm that the array slowly relaxes toward its equilibrium structure, which is obtained by minimizing the sum of the energy of edge dislocations and the layer compression energy. We revealed that the excess formation of edge dislocations in the initial stage is a consequence of local minimization of the elastic energy of the lamellar phase upon the contact of the two lamellar wetting layers. So the entire coarsening process can be viewed as a relaxation process from the local minimization to the global minimization of the elastic energy.

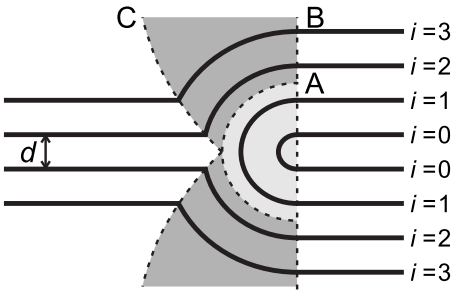

FIG. 13. Schematic cross-sectional structure of an edge dislocation ($\Delta n=4$). Shadowed areas correspond to curved layers. Dashed line B and curve C are the right and left boundaries between the curved and flat regions, respectively. Curve A is the boundary between the folded and the unfolded layers.

We also found characteristic elementary processes of the coarsening, which reflect the topology of the edge-dislocation network. The two elementary processes are (i) the motion of aligned nodes, which is caused via pairing of nodes, and (ii) topological relaxation of the network via collisions of two (aligned) nodes: The total length (and local number) of edge dislocations is decreased by the motion of m vs $m-1$ aligned nodes, which is the boundary structure between the region of m dislocations and that of $m-1$ dislocations, and it moves toward the region of m dislocations. The topology of the array, which is a network of edge dislocations, relaxes by the collision of two aligned nodes. We also revealed that the motion of aligned nodes is driven by the energy density difference across them. This was confirmed by comparing the measured velocity of the motion with the estimated energy difference, which is calculated using the model equilibrium structure.

Interestingly, the characteristic relaxation time of the total energy is ~ 10 h for $\phi=3-20$ wt %, independent of the concentration in this range.

We also found some other interesting phenomena in our experiments: Recombination of edge dislocations (the opposite process to the coarsening) using the perpendicular alignment of edge dislocations to the surface of a sponge droplet, edge-dislocation-array formation in an isolated lamellar domain, and migration of onion structures at the boundary between the homeotropic lamellar region and the onion-rich region.

These results may contribute to a deeper understanding of the dynamics of structural reorganization of defects in bulk under mechanical stress, and may be applied for manipulation of defect structures and network structure formation in ordered soft matter such as liquid crystals and colloids. The knowledge acquired here may directly be used to attain a perfect order in smectic liquid crystals and block copolymers under spatial confinement.

ACKNOWLEDGMENTS

This work was partly supported by a grant-in-aid from the Ministry of Education, Culture, Sports, Science and Technology, Japan.

APPENDIX A: STRUCTURE AND ENERGY OF AN EDGE DISLOCATION

1. Calculation of the geometric parameter g

We calculate the geometric parameter g, using a simple model of an edge-dislocation array. The structure is schematically shown in Fig. 13, in which we assume equidistance between adjacent layers (i.e., solid model). Curved layers are located in the shadowed areas enclosed by curve C and line B.

From the equidistance assumption, the curvature radius of the ith layer (see Fig. 13) in the curved area is $r_i=(i+1/2)d$, $(i=0,1,2\ldots)$. Here the lengths of the curved layers in the dark-shadowed region (enclosed by curves A and C and line B) are given by $r_i \cos^{-1}[1-(\Delta nd/2r_i)]$. Thus, ignoring the kinks on curve C for simplicity (cf. Fig. 1), we can estimate the curvature elastic energy per unit length of the edge dislocation as

$$w=\sum_{i=0}^{m}\frac{\pi\kappa}{2r_i}+\sum_{i=m+1}^{\infty}\frac{2\kappa}{r_i}\cos^{-1}\left(1-\frac{\Delta nd}{2r_i}\right)=\frac{\kappa}{d}g(\Delta n), \tag{A1}$$

where $m=\Delta n/2-1$ and the geometric parameter $g(\Delta n)$ is give by

$$g(\Delta n)=\sum_{i=0}^{m}\frac{\pi}{2i+1}+\sum_{i=m+1}^{\infty}\frac{2}{i+\frac{1}{2}}\cos^{-1}\left(1-\frac{\Delta n}{2i+1}\right). \tag{A2}$$

2. Core energy

Here we do not add the core energy E_c to Eq. (A1). E_c is necessary to calculate the energy of defects in thermotropic LCs since the curvature of a layer diverges at the core ($r=0$) and thus the core part, whose length scale is usually the molecular size, must be excluded from the calculation by introducing the cutoff radius r_c (e.g., [5,23]). In a hyperswollen lyotropic smectic phase, on the other hand, the core is occupied with a liquid (water in our case) and the curvature radius of the first layer (membrane) is much larger than the usual cutoff radius. As a result, for example, the tension of line defects of a hyperswollen lamellar phase coincides well with a model similar to Fig. 13 which does not take the core energy E_c into account [29].

3. The range of w

Next we estimate the range of w for the measured edge dislocation array in Fig. 4. $l\sim 20-80$ μm in Fig. 4(b) (3.0 wt %), 10–40 μm in Fig. 4(a) (10.0 wt %), and 10–30 μm in Fig. 4(c) (19.9 wt %). These correspond to $\Delta n=l/d\sim 4-12$ in Fig. 4(b), 6–24 in Fig. 4(a), and 12–36 in Fig. 4(c), respectively. For these ranges, we calculate $w_{\max}/w_{\min}=g(\Delta n_{\max})/g(\Delta n_{\min})$, using Eq. (A2) with the cutoff number of layers $i_{\max}=\Delta n/2+100$. This yields $w_{\max}/w_{\min}\simeq 1.2$ for all the three concentrations. In our study, thus, we can reasonably assume that w is almost constant with respect to l.

4. The energy cost of an elementary edge dislocation

Here we estimate the energy cost of an elementary edge dislocation. As mentioned above, when Δn is even number, the core is occupied by water and the curvature elastic energy does not diverge at the core. However, when Δn is an odd number, there should exist a membrane with an edge. Here we make a rough estimation of this energy cost of edge formation. For simplicity, we regard the edge as a semicylindrical structure of radius $\sim\delta/2$ and consider its curvature elasticity. Then the energy is estimated as $E_{\mathrm{edge}}\sim\pi\kappa_0/\delta$, where the elastic modulus should be the bare one. E_{edge} is about d/δ times larger than the energy required for folding a membrane with the radius of $d/2$ (the innermost layer of an even-Δn dislocation). This energy ratio is 40, 11, and 5.4 for 3.0, 10.0, and 19.8 wt %, respectively. This rough estimation suggests that the edge of a membrane may be avoided in the usual case, due to the large energy cost associated with edge formation.

Along the same line, we can calculate the curvature elastic energy of the edge dislocation of $\Delta n=1$ [$w(\Delta n=1)$] and compare it with $w(\Delta n=2)$. The model and calculation are basically the same as those for even Δn [see Fig. 13 and Eq. (A1)] except that the edge energy of a single layer is replaced with $E_{\mathrm{edge}}=\pi\kappa_0/\delta$. The ratio $w(1)/w(2)=55$, 8.6, and 4.0 for 3.0, 10.0, and 19.8 wt %, respectively. This large ratio means that $w(\mathrm{odd})>w(\mathrm{even})$ holds for a wide range of Δn, at least, in our experiments ($\Delta n<100$).

As described above, the edge of a membrane rarely exists in our experiments. However, such an elementary edge dislocation and the transition from $\Delta n=1$ to 2 in a wedge-shaped cell have been observed and studied in some LCs such as thermotropic, smectic, and cholesteric LCs [11,13,14]. For our lyotropic LC, by substituting the above $w(1)$ into Eq. (4) with our experimental conditions ($\tan\theta=0.02$ and $\phi\sim3-20$ wt %), the thickness below which the elementary edge dislocation is preferred is estimated as $n(\Delta n^*=1)<1$. Similarly, by substituting $w(2)$, we obtain the relation $n(\Delta n^*=2)\sim10$. These results suggest that the dislocation of $\Delta n=1$ is extremely unfavored due to its large core energy. Such defects might exist in a region whose thickness is about a few membranes, but practically it is very difficult to observe dislocations of $\Delta n=1$ or 2 in our experimental conditions.

It may be worth noting that this situation is roughly the same as in other LCs. Smalyukh *et al.* [13,14] showed in their study of a cholesteric LC that the transition of the Burgers vector from $p/2$ to p (p is the cholesteric pitch) occurs at the number of layers $n_c=h_c/p\simeq0.08/\theta=4$ for $\theta=0.02$. This is consistent with our estimation $n_c\sim1-10$. Bartolino *et al.* [11], on the other hand, showed in their study of thermotropic smectic LCs that the transition angle θ_c between $\Delta n=1$ and 2 is ~0.001 rad at $h=175$ μm and $d=3.0$ nm. Following the analytic relation between h and θ_c in [11], we obtain $h_c=0.44$ μm at $\theta=0.02$. This thickness corresponds to ~100 layers, which is about ten times larger than the corresponding value 1–10 in our estimation. Considering the difference in the model (e.g., the core energy) and the physical properties, however, this discrepancy should not be taken too seriously. Actually, if we calculate the coefficient of Eq. (4) with typical physical parameters of thermotropic LCs, $d\sim3$ nm, $B\sim10^7$ N/m^2, and $K\sim10^{-11}$ N, the resulting coefficient is of the same order as that of our system. Namely, the n-Δn relation is almost the same between our systems and typical thermotropic LCs in the framework of our simple model.

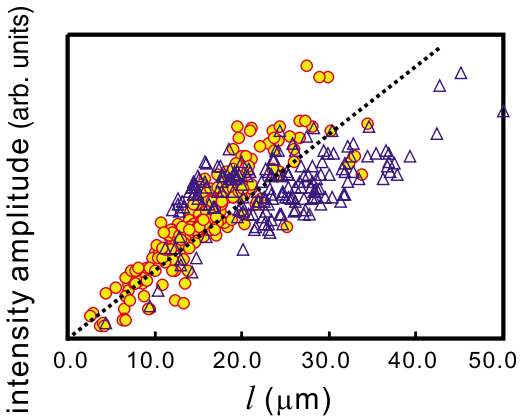

FIG. 14. (Color online) Dependence of the intensity amplitude of an edge dislocation on the width for $C_{10}E_3$-water, $\phi=10.0$ wt %, and $\tan\theta=0.018$. Circles correspond to the widths just after the formation and open triangles correspond to those at 77 h later. The dashed line is to guide the eye.

The increase of Δn, or Burgers vector, with the cell thickness has been studied in lyotropic, thermotropic, and cholesteric LCs as mentioned (e.g., [9–11,13,14]) and the formation of giant dislocations (large Δn) for weak constraint (for a large thickness) is also observed, e.g., in free-standing smectic films (e.g., [32,33]) and other systems (e.g., [34,35]). A characteristic feature of our study is that we experimentally study the dynamics for a much wider range of Δn than most previous studies on edge-dislocation arrays.

APPENDIX B: ESTIMATION OF THE WIDTH OF AN EDGE DISLOCATION

The width of an edge dislocation, l, which corresponds to the magnitude of its Burgers vector $|\mathbf{b}|$ [$=l\tan\theta=\Delta nd$; see Fig. 1(a)], cannot be measured directly in our observations, although the position of an edge dislocation x_e is easily measured. However, the intensity amplitude of an edge dislocation in optical microscopy images should reflect the structure; It increases monotonically with $|\mathbf{b}|$ for an image obtained with phase contrast microscopy, since the spatial gradient of the refractive index in a focal plane induces contrast and the steplike increase of the refractive index by an edge dislocation gives the intensity amplitude in the image. We also confirmed that the intensity amplitude of an edge dislocation is larger for one of wider spacings (e.g., Fig. 3). Thus, we can estimate the width l by making a proportional division of the spacings between an edge dislocation and the two neighboring ones using their intensity amplitudes, assuming the proportionality of the intensity amplitude to $|\mathbf{b}|$: x_e^i is the position of the ith edge dislocation, l_i is its width,

and I_i is its intensity amplitude. From this assumption, $l_i \propto \Delta n_i d \propto I_i$. The position of an edge dislocation is approximated by the center of the width l ($x_{i+1}-x_e \simeq x_e - x_i \simeq l/2$) since the wedge angle is small in our experiments ($\tan\theta \simeq 0.02$) [22]. Therefore, the width is estimated as

$$l_i = \frac{I_i}{I_i + I_{i+1}}(x_e^{i+1} - x_e^i) + \frac{I_i}{I_{i-1} + I_i}(x_e^i - x_e^{i-1}). \quad \text{(B1)}$$

We show the relation between the intensity amplitude and the estimated width in Fig. 14.

[1] P. M. Chaikin and T. C. Lubensky, *Principles of Condensed Matter Physics* (Cambridge University Press, Cambridge, U.K., 1995).
[2] A. J. Bray, Adv. Phys. **43**, 357 (1994).
[3] Y. Iwashita and H. Tanaka, Phys. Rev. Lett. **95**, 047801 (2005).
[4] D. Caillard and J. L. Martin, *Thermally Activated Mechanisms in Crystal Plasticity* (Elsevier, Amsterdam, 2003).
[5] M. Kleman and O. D. Lavrentovich, *Soft Matter Physics: An Introduction* (Springer, New York, 2003).
[6] M. J. Whelan, P. B. Hirsch, R. W. Horne, and W. Bollmann, Proc. R. Soc. London, Ser. A **240**, 524 (1957).
[7] J. A. Moriarty, V. Vitek, V. V. Bulatov, and S. Yip, J. Comput. Aided Mater. Des. **9**, 99 (2002).
[8] P. Schall, I. Cohen, D. A. Weitz, and F. Spaepen, Science **305**, 1944 (2004).
[9] F. Nallet and J. Prost, Europhys. Lett. **4**, 307 (1987).
[10] C. E. Williams, and M. Kleman, J. Phys. (Paris), Lett. **35**, L33 (1974).
[11] R. Bartolino and G. Durand, Mol. Cryst. Liq. Cryst. **40**, 117 (1977).
[12] R. B. Meyer, B. Stebler, and S. T. Lagerwall, Phys. Rev. Lett. **41**, 1393 (1978).
[13] I. I. Smalyukh and O. D. Lavrentovich, Phys. Rev. E **66**, 051703 (2002).
[14] I. I. Smalyukh and O. D. Lavrentovich, Phys. Rev. Lett. **90**, 085503 (2003).
[15] I. Lelidis, M. Kleman, and J. L. Martin, Mol. Cryst. Liq. Cryst. Sci. Technol., Sect. A **330**, 457 (1999).
[16] I. Lelidis, M. Kleman, and J. L. Martin, Mol. Cryst. Liq. Cryst. **351**, 187 (2000).
[17] C. Blanc, N. Zuodar, I. Lelidis, M. Kleman, and J. L. Martin, Phys. Rev. E **69**, 011705 (2004).
[18] P. Kekicheff and H. K. Christenson, Phys. Rev. Lett. **63**, 2823 (1989).
[19] D. A. Antelmi, P. Kekicheff, and P. Richetti, Langmuir **15**, 7774 (1999).
[20] D. Roux, C. Coulon, and M. E. Cates, J. Phys. Chem. **96**, 4174 (1992).
[21] H. Tanaka, M. Isobe, and J. Yamamoto, Phys. Rev. Lett. **89**, 168303 (2002).
[22] P. Richetti, P. Kekicheff, and P. Barois, J. Phys. II **5**, 1129 (1995).
[23] R. Holyst and P. Oswald, Int. J. Mod. Phys. B **9**, 1515 (1995).
[24] T. D. Le, U. Olsson, K. Mortensen, J. Zipfel, and W. Richtering, Langmuir **17**, 999 (2001).
[25] Y. Iwashita and H. Tanaka, Nat. Mater. **5**, 147 (2006).
[26] R. Strey, R. Schomäcker, D. Roux, F. Nallet, and U. Olsson, J. Chem. Soc. **86**, 2253 (1990).
[27] J. Yamamoto and H. Tanaka, Phys. Rev. Lett. **77**, 4390 (1996).
[28] W. Helfrich, Z. Naturforsch. A **33**, 305 (1978).
[29] Y. Iwashita and H. Tanaka, Phys. Rev. Lett. **90**, 045501 (2003).
[30] A. M. Alsayed, M. F. Islam, J. Zhang, P. J. Collings, and A. G. Yodh, Science **309**, 1207 (2005).
[31] Y. Iwashita and H. Tanaka, Phys. Rev. Lett. **98**, 145703 (2007).
[32] P. Oswald, P. Pieranski, F. Picano, and R. Holyst, Phys. Rev. Lett. **88**, 015503 (2001).
[33] P. Oswald, F. Picano, and F. Caillier, Phys. Rev. E **68**, 061701 (2003).
[34] M. Kleman, C. E. Williams, M. J. Costello, and T. Gulik-krzywicki, Philos. Mag. **35**, 33 (1977).
[35] A. Asher and P. S. Pershan, Biophys. J. **27**, 393 (1979).